A Numerical Simulation of the Two-Day Wave near the Stratopause

VARAVUT LIMPASUVAN AND CONWAY B. LEOVY

Department of Atmospheric Sciences, University of Washington, Seattle, Washington

YVAN J. ORSOLINI

Norwegian Institute for Air Research, Kjeller, Norway

BYRON A. BOVILLE

National Center for Atmospheric Research, Boulder, Colorado

(Manuscript received 5 October 1998, in final form 22 July 1999)

ABSTRACT

The middle atmosphere version of the National Center for Atmospheric Research Community Climate Model 2 (MACCM2) mechanistic model is used to simulate several aspects of the observed two-day wave near the stratopause and its possible connection with inertial instability. Model experiments show that, for a prescribed initial wind condition with strong horizontal wind variation in the Tropics, inertial instability can trigger the two-day wave. An increase in horizontal wind curvature fostered by inertial instability circulation barotropically destabilizes the easterly jet in low summer latitudes and allows first the growth of the wavenumber-4 and then the wavenumber-3 component of the two-day wave. Near the stratopause, the two-day wave Eliassen–Palm flux is directed equatorward away from the wave's critical line source and westerly momentum is transported into the easterly jet core by the wave. While much of the wavenumber-4 energy is confined near the stratopause, the wavenumber-3 energy can propagate upward well into the mesosphere where strong Rayleigh damping is imposed. The model results suggest that the observed disparity in the wavenumber-3 amplitude between the austral and boreal summers is a consequence of the difference in summer easterly jet strength.

1. Introduction

Recent studies by Limpasuvan et al. (2000) and Orsolini et al. (1997) using the *Upper Atmosphere Research Satellite* (*UARS*) Microwave Limb Sounder (MLS) temperature data and the United Kingdom Meteorological Office (UKMO) stratospheric analyses, respectively, suggest an intriguing connection between inertial instability and the two-day wave near the stratopause. As observed by Hayashi et al. (1998) and Hitchman et al. (1987), vertically stacked temperature anomalies associated with inertial instability appear around the solstice near the winter subtropical stratopause. These features are believed to be organized by midlatitude winter Rossby waves as they meridionally propagate toward the strong cross-equatorial wind shear zone organized by the mean residual circulation (O'Sullivan and Hitchman 1992; Sassi et al. 1993). Inertial instability circulation transports westerly momentum across the equator; as a result, zonal momentum is redistributed and positive horizontal curvature of the easterly wind profile in the summer subtropics tends to increase. In some instances after the solstice, through such momentum redistribution and increased wind curvature, the subtropical easterly jet can become barotropically unstable, giving rise to the two-day wave. During the 1992–93 austral summer observed by Limpasuvan et al. (2000), inertial instability and its mean flow effects are suggested to initiate the barotropically unstable two-day wave features. The relevance of this triggering mechanism near the stratopause remains, however, a wide-open question.

In other instances, the two-day wave appears to be generated by baroclinic instability above the summer easterly jet core where the vertical wind curvature and/or shear can be large (Wu et al. 1996; Limpasuvan et al. 2000). In these situations, easterly jet barotropic destabilization by inertial instability may not be relevant to the onset of the two-day wave. Instead, zonal wind drag imposed by breaking gravity waves in the lower mesosphere may be the most immediate factor in creating the unstable zonal mean wind distribution, as first

Corresponding author address: Varavut Limpasuvan, Department of Atmospheric Sciences, University of Washington, Box 351640, Seattle, WA 98195.
E-mail: var@atmos.washington.edu

suggested by Plumb (1983). Using the U.K. University Global Atmospheric Modeling Program (UGAMP) model, Norton and Thuburn (1996, 1997) simulated a realistic two-day wave generated by this mechanism. They also experimented with replacing the gravity wave drag parameterization by simple Rayleigh friction. In this case, the two-day wave was either absent or appeared far from where it is observed.

In this paper, we explore the generation of the two-day wave by the mechanism of barotropic instability fostered by inertially unstable disturbances. The hypothesized connection between the two-day wave and inertial instability is supported by results from a mechanistic version of a middle atmosphere general circulation model (GCM). Inertial instability features act to trigger the two-day wave in the model through easterly jet destabilization if an initial condition is prescribed with strong horizontal wind shear. Although not all aspects of the observed two-day wave are reproduced, the simulated two-day wave does show some degree of realism. The simulated wave's sensitivity to the initial zonal flow structure also provides some insights into the variability of the observed wave. We do not discount the importance of gravity waves. Their role in establishing the zonal mean field in which the two-day wave flourishes is implicit in our model results.

2. Model description

The model is adapted from the National Center for Atmospheric Research (NCAR) Middle Atmosphere version of the Community Climate Model 2 (MACCM2). Takahashi and Boville (1992) presented a study of the quasi-biennial oscillation (QBO) using a similar mechanistic model based on a preliminary version of the NCAR Community Climate Model 2 (CCM2). Details of the CCM2 and MACCM2 are discussed in Hack et al. (1993) and Boville (1995), respectively.

The model solves the three-dimensional primitive equations by invoking the spectral transform method in the horizontal and a finite-difference scheme in the vertical. To save computational resources, a "T21 $\times$ 10" trapezoidal truncation scheme is used. This scheme has the same meridional resolution as the standard T21 scheme, but the zonal resolution is reduced by half (see Boville 1995). Thus, there are 32 Gaussian grid points in the meridional direction and 32 evenly spaced grid points in the zonal direction. The model has 47 vertical levels ranging from 234.57 to 0.004 hPa (about 10–87 km). For a scale height of 7 km, the level separation in log pressure coordinate is 1.4 km at the lower boundary and 1.7 km at the model's top. The model integration time step is 24 min and results are archived every 12 h. At all levels, a biharmonic (∇^4) horizontal diffusion is applied with a constant coefficient value of 1.0×10^{16} m^4 s^{-1}. The vertical diffusion parameterization depends on the local Richardson number, and a minimum diffusivity of 0.01 m^2 s^{-1} is assumed for stable conditions in the middle atmosphere.

Cooling to space is approximated by a Newtonian cooling scheme that relaxes the model temperature to the zonally symmetric initial condition discussed below. The damping rate of the cooling coefficient (K_n) varies only in height (z) roughly from 23 days at the lower boundary to less than 5 days near the model top. The coefficient profile is given by

$$K_n = 1.0 \times 10^{-6}\ \mathrm{s}^{-1}\left[\alpha + \beta \tanh\left(\frac{z - 35\ \mathrm{km}}{7\ \mathrm{km}}\right)\right], \quad (2.1)$$

where (α, β) is specified during the model experiments. This cooling scheme is somewhat artificial but is necessary to keep the model from deviating too far from the initial condition. It also allows for the examination of relationships between the observed zonal flow (and some modest variations of it) and the various resulting waves in a relatively straightforward manner.

The mean flow effects of gravity waves are approximated by simple Rayleigh friction. The scheme takes on a linear drag form in the momentum equation with the frictional coefficients varying only in height. The coefficient is given as

$$K_r = \frac{2}{3}\ \mathrm{day}^{-1}\left[1.0 + \tanh\left(\frac{z - 80\ \mathrm{km}}{5\ \mathrm{km}}\right)\right]. \quad (2.2)$$

Rayleigh friction crudely emulates the decelerative effect of breaking gravity waves in the mesosphere in closing the jets. Since it is applied to the total wind field, it damps both the mean wind and wave variations above 70 km. Consequently, the upper model levels where Rayleigh friction is effective serve as sponge layers to prevent reflection of extraneous waves that would otherwise arise from wave reflection due to the rigid lid upper boundary condition (Andrews et al. 1987). The model's top and the sponge layers are above most of the interesting simulated features presented in the next sections.

The model's initial wind field is zonally symmetric and specified analytically (see section 3). The corresponding initial temperature is derived from the initial zonal wind field using the thermal wind relation (Andrews et al. 1987). To facilitate the derivation, a vertical temperature profile at the equator is specified according to the *U.S. Standard Atmosphere, 1976.* The profile serves as a set of integration constants that allow the wind field to be integrated separately in each hemisphere to obtain the temperature field. The initial fields are first computed in an evenly spaced coordinate system. The latitude coordinate ranges from $-90°$ to $90°$ in intervals of $1°$. In the vertical, log pressure coordinate is used covering heights of 10–90 km in increments of 1 km. The fields are then interpolated onto the model coordinates.

Given an initial condition, a stationary, zonal wavenumber-1 forcing is imposed at the model's base ($\sim$10

km or 235 hPa) in the winter hemisphere. In reality, winter wave forcing is generated near the ground through topographical variations and land–sea thermal contrast. Only the largest zonal scale and the lowest frequency wave can propagate into the middle atmosphere because of the filtering nature of the troposphere (Charney and Drazin 1961; Andrews et al. 1987). The forced wave is expected to propagate upward through much of the lower stratosphere and then veers equatorward near the stratopause region where it is mechanically and/or thermally damped. Signals of planetary waves in low winter latitudes are observed in the *UARS* MLS observations (Limpasuvan et al. 2000) and the Cryogenic Limbs Array Etalon Spectrometer (CLAES) observations (Hayashi et al. 1998).

The forcing is accomplished through the geopotential field. The total geopotential field at the model's base (near the tropopause) consists of the wave perturbation forcing, $\Phi'(\lambda, \varphi, t)$, in addition to the stationary, zonally symmetric forcing, $\overline{\Phi}(\varphi)$, which is in hydrostatic balance with the initial temperature. The wave perturbation is described analytically and is slowly turned on from the model initial time (model day 0) reaching its steady peak amplitude by model day 20. The geopotential perturbation is focused in the winter hemisphere and is given as a product of a spatial function, F, and temporal function, G:

$$\Phi' = \begin{cases} F(\lambda, \varphi)G(t) & \text{for } 30^\circ \le \varphi \le 82.5^\circ \\ 0 & \text{for other } \varphi, \end{cases}$$

where

$$F(\lambda, \varphi) = \left\{ \sin\left[\pi \left(\frac{|\varphi| - 30^\circ}{60^\circ - \dfrac{(|\varphi| - 60^\circ)}{3}} \right) \right] \right\}^2 \cos\left(\frac{\pi}{180^\circ} \lambda \right)$$

and

$$G(t) = A\left[1.0 - \exp\left(-\frac{t}{\tau} \right) \right].$$

Here, λ, φ, and t represent longitude, latitude, and time, respectively. The parameter τ is fixed at 2.5×10^5 s. By model day 10, the forcing amplitude $G(t)$ already exceeds 90% of its constant peak value, A, which is varied in the sensitivity runs (section 6). The function F describes a zonal wavenumber-1 perturbation centered at 60° in the winter hemisphere with 30° width and nodes at 90° and 270°E longitudes.

3. Control run: General features

The control run results will first be discussed. In this run, the weakest planetary wave forcing amplitude is specified ($A = 368$ m^2 s^{-2}), and the Newtonian cooling profile with the constants (α, β) = (3.0, 2.5) are used.

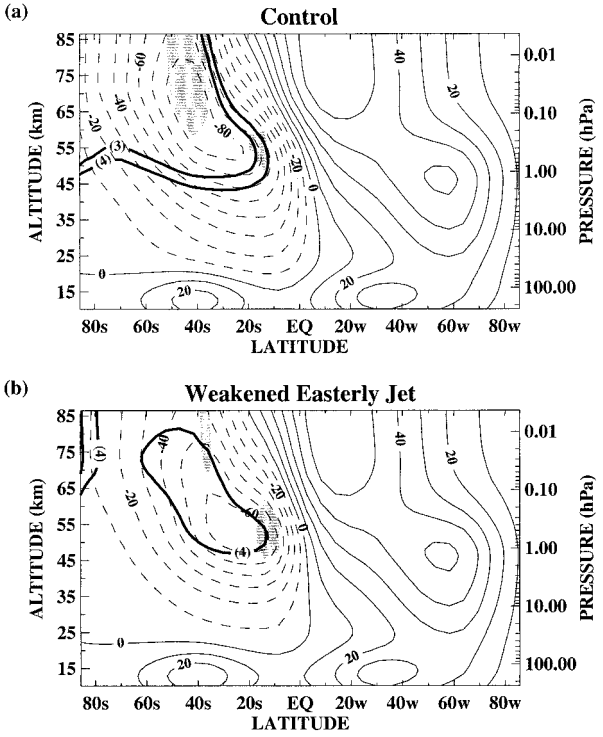

FIG. 1. (a) Initial zonal wind (in m s^{-1}) of the control run. The shaded areas represent regions where the necessary condition for barotropic–baroclinic instability is satisfied ($\overline{q}_\varphi \le 0$), and the bold lines labeled with "3" and "4" locate the critical lines for the (3, 2.0) and (4, 1.8) modes of the observed two-day wave. (b) Same as (a) but for the weakened initial easterly jet case. The (3, 2.0) critical line is not supported by the zonal flow in this case. Note: In this figure and the rest of this paper, latitudes in the winter (summer) hemisphere are denoted with the letters "w" ("s"); for example, "20w" and "20s" represent 20° latitude in winter and summer hemisphere, respectively.

a. Initial zonal wind condition

The model's initial state for the control run is designed to emulate the atmospheric conditions under which the two-day wave flourishes. Shown in Fig. 1a, the initial wind condition is prescribed analytically (see Limpasuvan 1998) to mimic the main characteristics of the observed, near-solstice austral summer wind structure derived from MLS temperatures by Limpasuvan et al. (2000). The equatorial stratopause region is characterized by the easterly phase of the semiannual oscillation and a descending westerly shear zone (as observed by Hitchman and Leovy 1986). Likewise, the presence of strong equatorial horizontal wind shear near the stratopause allows the zonally symmetric necessary condition for *inertial instability* to be satisfied (also observed by Ray et al. 1998): $f(f - a^{-1}\overline{u}_\varphi) < 0$, where f, a, and $\overline{u}_\varphi$ are the Coriolis parameter, the earth's radius, and the partial derivative of the zonal mean zonal wind with respect to latitude. Strong vertical wind variations above the easterly jet core and strong horizontal wind curvature on the equatorward flank of the easterly jet

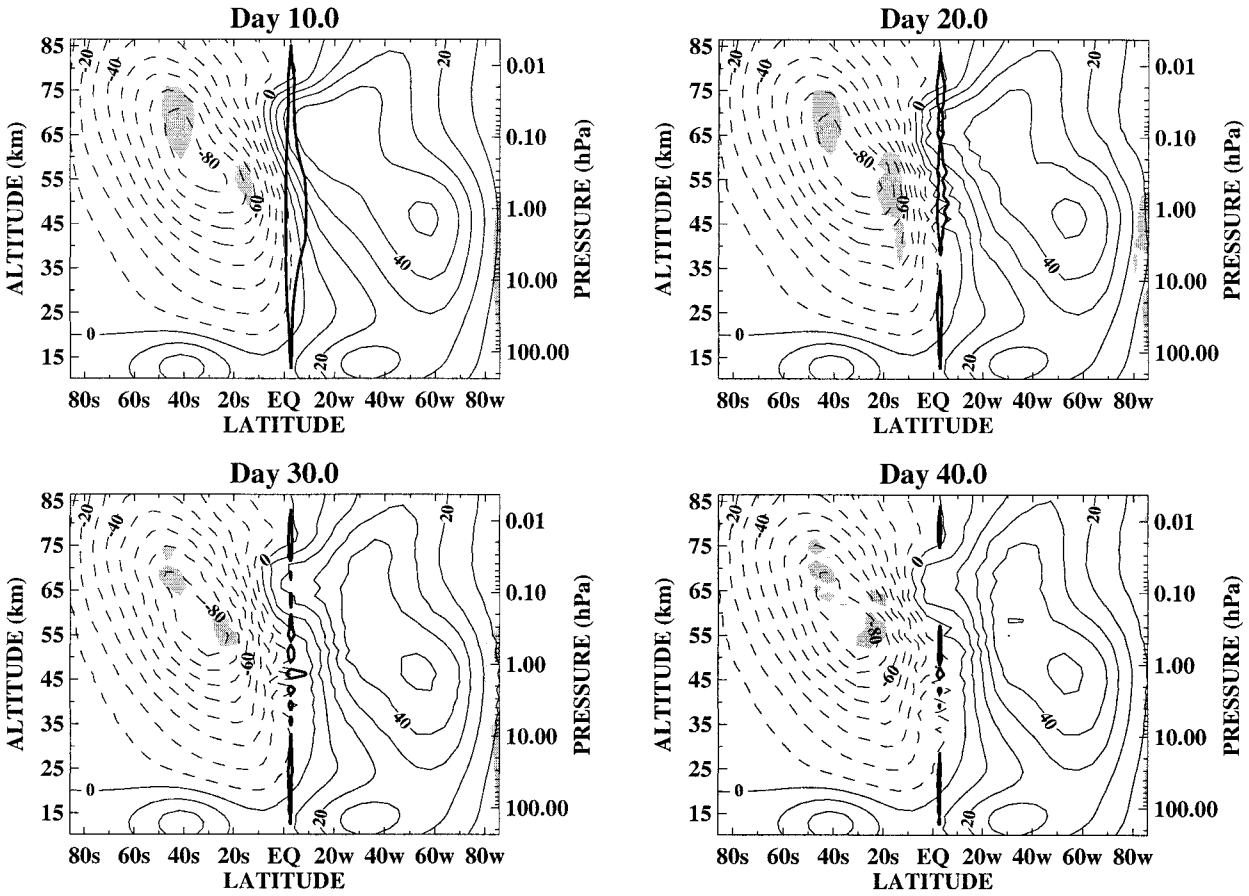

FIG. 2. The zonal mean zonal wind cross sections of the control run. The contours are in increments of 10 m s^{-1}. The shaded areas show where $\overline{q}_\varphi \leq 0$. The bold line in the equatorial region encloses the area where $f(f - a^{-1}\overline{u}_\varphi) < 0$, denoting the region where the necessary condition for inertial instability is fulfilled.

are responsible for a large region of quasigeostrophic potential vorticity meridional gradient ($\overline{q}_\varphi$) reversal above 60 km and a small region in the summer subtropics (shaded regions in Fig. 1a). In the lower stratosphere (below 35 km), the equatorial flow is prescribed to be in the easterly QBO phase. O'Sullivan and Hitchman (1992) have used a similarly prescribed wind structure to simulate inertially unstable wave development in their mechanistic model.

Limpasuvan et al. (2000) find that the strong austral summer easterly jet can support the critical lines (where the wave phase speed matches the background wind) of both two-day wave components near negative $\overline{q}_\varphi$ regions. For reference, these critical lines are also shown in Fig. 1a as bold lines for mode (3, 2.0) and (4, 1.8) observed in the MLS data. Here, the first number in the parenthesis represents the zonal wavenumber, while the second number represents the dominant period (in days) from which the mode phase speed is determined. The critical lines are shown only to demonstrate the similarity between the prescribed initial winds and the observed austral summer conditions. These modes may not necessarily be generated in the model runs.

In general, preexisting thermal and dynamical forcing and associated mean meridional circulations are responsible for setting up this near-solstitial mean atmospheric condition. To maintain this favorable condition for the two-day wave, the model state is continually "nudged" back to the initial state through the strong Newtonian cooling. This maintenance of the zonal wind structure is expected to break down if the mean wind is strongly affected by wave–mean flow interaction during a model run or in a region where the strongly imposed Rayleigh friction acts to decelerate the mean wind at all latitudes. The region affected by Rayleigh friction is above 70 km and reasonably far from the location of in situ wave generation in the model. However, effects from the upper boundary conditions may still influence the model results.

b. Zonal mean wind evolution

Evolution of the zonal mean zonal wind distribution is shown in Fig. 2. By day 10, the structure below 0.10 hPa (~65 km) remains similar to the initial wind due to the strong Newtonian cooling above 1.0 hPa and the

weak Rayleigh friction below 0.1 hPa. The negative $\overline{q}_\varphi$ region (shaded area) in the low summer latitudes remains small. Above 0.10 hPa, the mean wind has experienced the decelerative effects of the Rayleigh friction parameterization that partially mimics the role of breaking gravity waves in the mesosphere. Subsequently, some of the initially prescribed negative $\overline{q}_\varphi$ region near 40° summer latitude has disappeared. The strong meridional wind shear above 0.1 hPa (Fig. 1a) has also diminished as a result of Rayleigh friction. A potential region of inertial instability where $f(f - a^{-1}\overline{u}_\varphi) < 0$ (enclosed by the bold line) is seen near the stratopause in the winter subtropics.

Zonal mean zonal winds subsequently change mainly within 30° latitude of the equator. In low summer latitudes, the negative $\overline{q}_\varphi$ region has expanded meridionally and vertically by day 20, extending well below 2.0 hPa. Increased meridional wind shear on the summer side of the equator together with reduced equatorial wind shear is responsible for this expansion. As a result, the size of the inertially unstable region has decreased. After day 20, the low summer latitude negative $\overline{q}_\varphi$ region shifts toward higher latitude, closer to the easterly jet core. Around 1.0 hPa, this region completely disappears. The equatorial wind shear becomes notably weak, consistent with the dwindling regions of possible inertial instability. The easterly wind has also intruded farther across the equator around the stratopause.

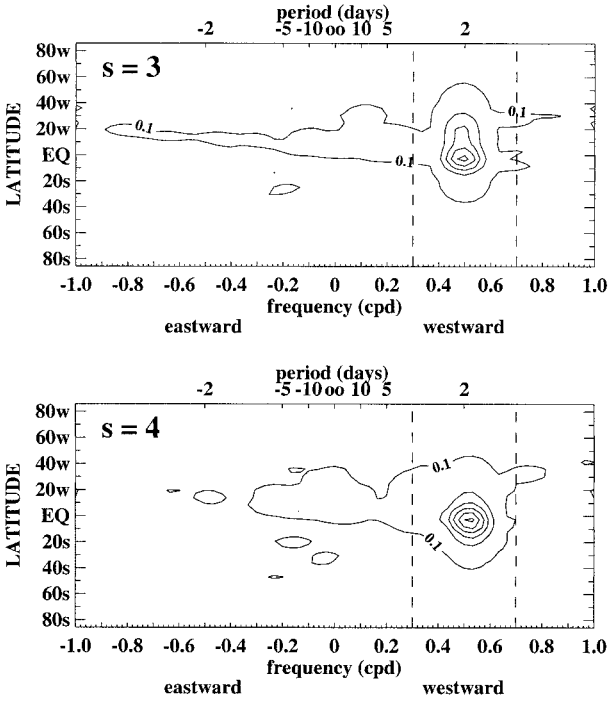

FIG. 3. The latitude–frequency structure of the meridional wind zonal wavenumbers -3 and -4 spectra at 0.3 hPa of the control run. The contours are given in increments of 0.2 $m^2 s^{-2}$ day. The dashed lines define the frequency interval 0.3–0.7 cpd.

4. Control run: Two-day wave features

Conventional spectral analysis (e.g., Hayashi 1971) is used to identify the simulated two-day wave. The computation is performed using a 30-day windowed twice-daily time series spanning model days 10 to 39. The spectral resolution is then about 0.03 cycles per day (cpd). Both meridional wind and temperature fields are analyzed.

Above 1.0 hPa, wavenumber–frequency spectral diagrams reveal that the low summer latitude wave disturbance in the simulation is dominated by zonal wavenumber-3 and -4 components corresponding to those of the observed two-day wave (not shown). The latitude–frequency structure of the meridional wind field at 0.3 hPa is given in Fig. 3 for zonal wavenumbers 3 and 4. Spectral amplitudes are strongest at the equator and peak at westward-propagating periods of 2.04 days (~0.49 cpd) and 1.89 days (~0.53 cpd), respectively. The slightly weaker wavenumber-3 signature is more skewed toward low winter latitudes than the wavenumber 4. Spectral analysis of the temperature field reveals similar dominant wavenumber-3 and -4 features in the resolved spectra with peaks near 0.49 and 0.53 cpd (not shown). However, unlike the meridional wind spectra, the temperature spectral peaks are concentrated near 10° summer latitude (see Fig. 4).

To examine the spatial–temporal structure of the identified disturbances, bandpass filtering of these spectral signals is performed over the frequency band ranging from 0.3 to 0.7 cpd (dashed lines in Fig. 3). By definition, the disturbances associated with the filtered zonal wavenumber-3 and -4 signal are referred to as the ''(3, 2.04)'' and ''(4, 1.89)'' modes, which is analogous to the wave definitions used by Limpasuvan et al. (2000).

a. Two-day amplitude structure

Time-averaged cross-section structures of the (4, 1.89) and (3, 2.04) modes are presented in Figs. 4a,b for both temperature and meridional wind. Averaging is performed during days 20–30 for the (4, 1.89) mode and days 25–35 for the (3, 2.04) mode when each mode amplitude is strongest (shown later in Fig. 6). Meridional wind amplitude for both modes is centered near the stratopause and over the equator. The (3, 2.04) mode extends upward more than the (4, 1.89) mode and is tilted slightly toward the summer hemisphere. Temperature amplitudes for both waves are centered in the upper stratosphere and lower mesosphere in the summer Tropics, and both waves have nodes near 55 km. Temperature amplitude of the (3, 2.04) mode is large in the upper mesosphere despite the strong Rayleigh damping there, and it is shifted slightly poleward relative to the (4, 1.89) mode.

Although the occurrence of these modes' wavenumbers, frequencies, and location parallels the obser-

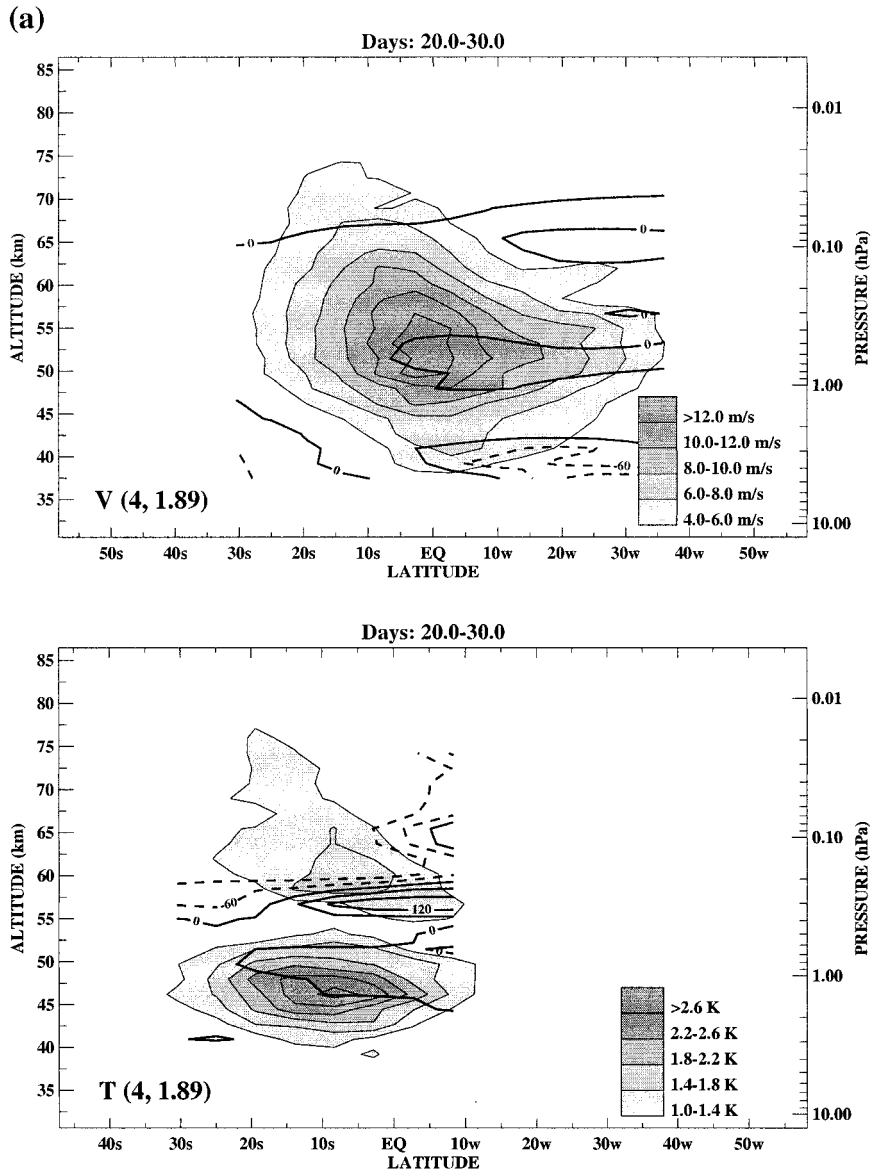

FIG. 4. (a) The time-averaged cross section of the (4, 1.89) mode of the control run. The averaging is done for model days 20–30. The meridional wind amplitude (top) is contoured every 2 m s^{-1}, and the temperature amplitude (bottom) is contoured every 0.2 K. The phase lines are shown as bold contours in increments of 60°.

vations, model features differ from the observations in several respects: the temperature node with vertical phase reversal near 55 km, the absence of a weak temperature feature in the winter hemisphere in antiphase with the summer hemisphere feature, and smaller meridional width and amplitude of the meridional wind in the upper mesosphere (e.g., Muller and Nelson 1978; Vincent 1984; Wu et al. 1993, 1996; Limpasuvan et al. 2000). These discrepancies may be primarily attributable to model limitations, especially the strong Rayleigh and Newtonian damping near the rigid lid. Finally, below 65 km, amplitudes of both wavenumber-3 and -4 components are comparable in the simulation. In the observations, comparable amplitudes of the modes are only observed during the 1993–94 austral summer MLS case of Limpasuvan et al. (2000) and the 1979 austral summer Limb Infrared Monitor of the Stratosphere (LIMS) temperature of Burks and Leovy (1986).

b. Two-day wave EP flux

The time-averaged, filtered Eliassen–Palm (EP) fluxes for the (3, 2.04) and (4, 1.89) modes are shown in Fig. 5. As defined by Andrews et al. (1987), the EP flux vector components are computed by bandpass filtering (between 0.30 and 0.70 cpd) for zonal wave-

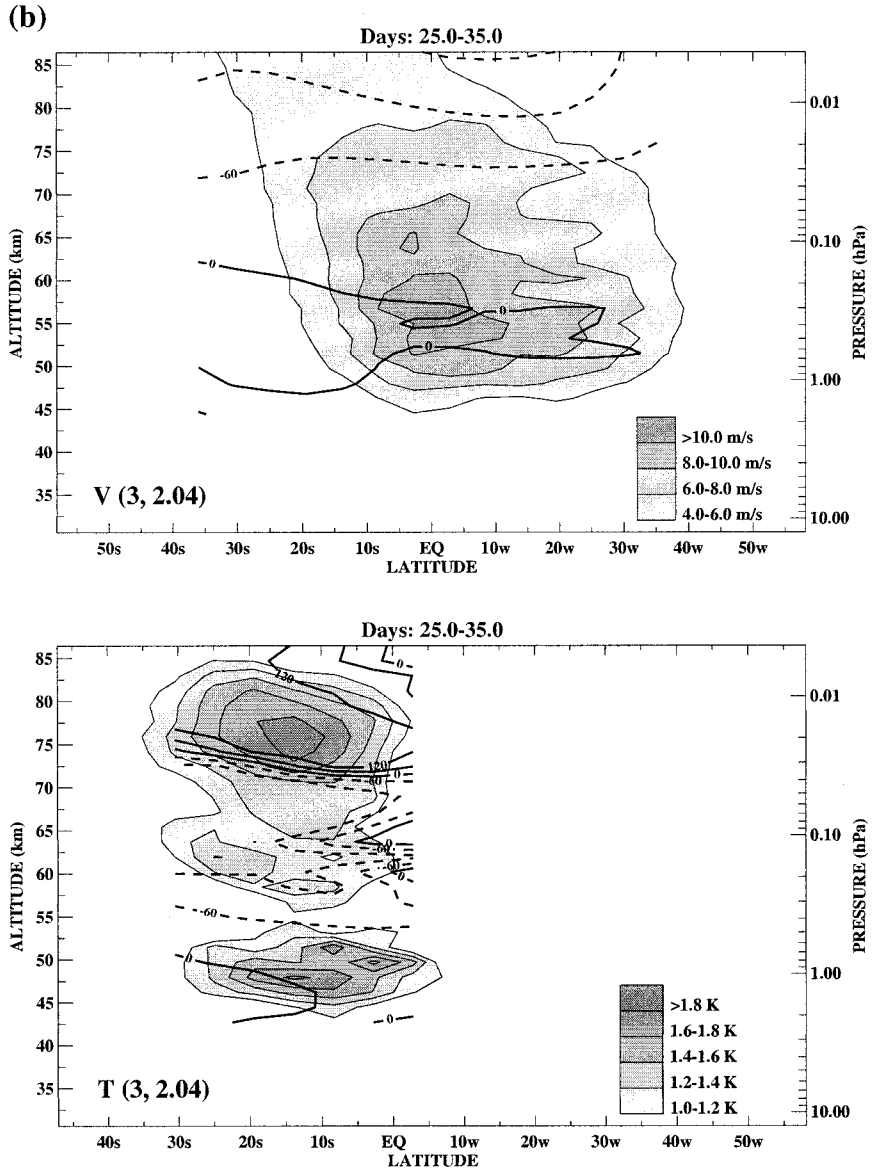

FIG. 4 (*Continued*) (b) Same as (a) except for the (3, 2.04) mode. Also, the averaging is done instead for model days 25–35.

numbers 3 and 4. Each component is scaled by $(\rho_0 a \cos\varphi)^{-1}$, where ρ_0 is the basic density profile. In addition, the vertical vector component is scaled by the ratio of the displayed horizontal distance to the displayed vertical distance. The mode critical line (bold line) is also plotted along with the averaged negative $\overline{q}_\varphi$ region (shaded area). The mode phase speed is computed from its central period (i.e., 2.04 and 1.89 days), as indicated by the spectral analysis (Fig. 3). The time averaging is performed over days 20–30 and 15–25 for the (3, 2.04) and (4, 1.89) modes, respectively. These 10-day periods encompass the time frame when the modes are growing and beginning to reach their peaks (shown later in Fig. 6).

The EP flux vectors suggest that growth of both modes can be attributed to the wave instability mechanism. The (4, 1.89) mode growth that appears first in the model exhibits the largest EP flux between 0.10 and 1.0 hPa, which is mainly directed horizontally toward the winter hemisphere. The EP flux vectors appear to emanate from the mode's critical line, which resides in the negative $\overline{q}_\varphi$ region, suggesting that the critical line serves as a localized source of wave activity (cf. Salby 1996, p. 522). This local generation of EP flux is consistent with barotropic instability growth near the critical line. The zonal wind forcing of the (4, 1.89) mode, as large as 1 m s^{-1} day^{-1} in the averaged period, transfers westerly momentum into the easterly jet core, weak-

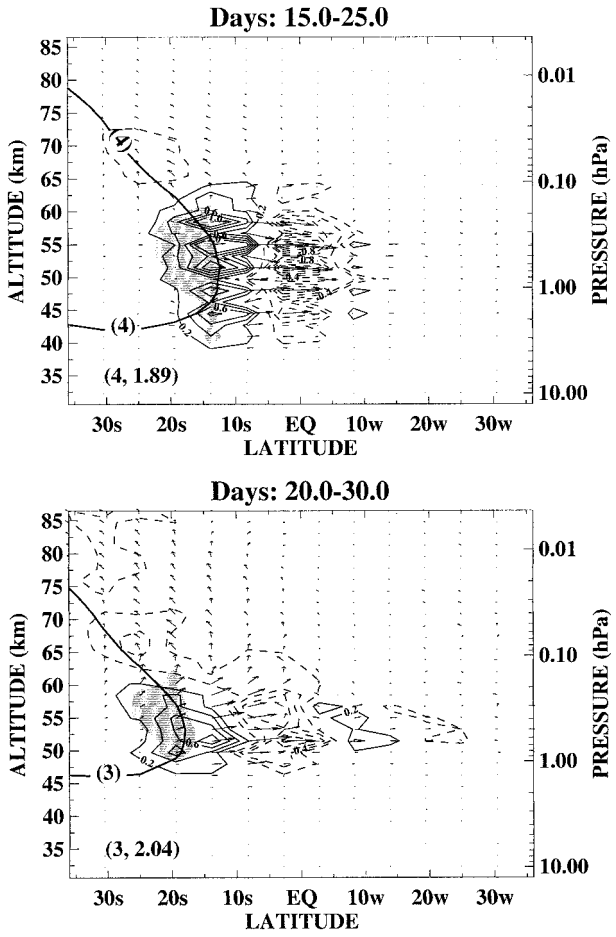

FIG. 5. The 10-day-averaged EP flux vector diagrams for (top) the (4, 1.89) mode, (bottom) and the (3, 2.04) mode of the control run. The maximum vector length of the bottom panel is scaled relative to the top panel. The wave forcing per unit mass (EP flux divergence) is contoured every 0.2 m s^{-1} day^{-1}. Solid (dashed) contours denote westerly (easterly) acceleration. The shaded area shows the averaged negative $\overline{q}_\varphi$ region. The mode critical line is shown in the diagrams as a bold line and labeled with "3" and "4" for the (3, 2.04) and (4, 1.89) modes, respectively.

ening the easterly mean wind around 10° summer latitude and strengthening the easterly mean wind over the equator. Above 0.1 hPa, there is weak upward–poleward energy propagation along the critical line.

The (3, 2.04) mode EP flux also appears to emanate from its critical line within the negative $\overline{q}_\varphi$ region, which is centered near 20° summer latitude during days 20–30 (Fig. 5, bottom). Near the stratopause, the strength of wave fluxes is comparable to the (4, 1.89) mode. Like the (4, 1.89) mode, the associated forcing with magnitude of roughly 0.8 m s^{-1} day^{-1} near the stratopause tends to transport westerly momentum farther toward the easterly jet core. Unlike the (4, 1.89) mode, the (3, 2.04) upward–poleward energy propagation penetrates into the upper mesosphere where the model is highly damped. This strong vertical propagation pattern corresponds to the noted (3, 2.04) disturbance amplitude shown in Fig. 4b above 0.1 hPa.

c. Two-day wave amplitude evolution

Figure 6a shows the (4, 1.89) meridional wind amplitude and zonal mean wind evolution at 0.3 hPa. Around days 13–20, the (4, 1.89) mode begins to grow as its critical line is present in the negative $\overline{q}_\varphi$ region over a deep layer [Fig. 5 (top) and Fig. 2 (upper right)]. By day 20, the amplitude becomes large, and associated wave fluxes begin to alter the mean flow, limiting further wave growth. Subsequent to maximum wave amplification (day 22), the critical line shifts summerward, while the zero wind line translates winterward. This broadening and weakening of the equatorward flank of the easterly jet is consistent with the zonal wind forcing shown in Fig. 5. The altered mean flow displaces the negative $\overline{q}_\varphi$ region to higher latitude after day 20. A second growth episode then appears and peaks around day 27. This second growth phase may be related to the continued intersection of the critical line source region with the displaced negative $\overline{q}_\varphi$ region. Amplitude saturation of the secondary wave episode coincides with the farther poleward shift of the negative $\overline{q}_\varphi$ region.

Figure 6b shows the (3, 2.04) meridional wind amplitude and mean wind evolution at 0.3 hPa. The growth of the (3, 2.04) mode appears after day 20 when its critical line appears well within the poleward displaced negative $\overline{q}_\varphi$ region over a deep layer. The growing amplitude maximizes around day 30, and the associated zonal wind forcing is consistent with the zonal wind evolution. After day 25, gradual divergence of the zero and -70 m s^{-1} isopleths away from the equator is readily observed and, at the same time, the pattern of EP flux indicates westerly momentum flux into the easterly jet core (Fig. 5, bottom). Since the (3, 2.04) and (4, 1.89) modes have significant amplitudes between days 25 and 30, the mean flow can be affected by forcing from both modes.

We emphasize that the crucial correspondence that indicates wave instability is not between the negative $\overline{q}_\varphi$ regions and wave amplitude but rather between these regions and EP flux divergence, as depicted in Fig. 5. However, wave amplitude that can be readily computed from observations (as done in Wu et al. 1996 and Limpasuvan et al. 2000) can, to a first order, help diagnose a wave instability signature particularly during the wave's initial growth phase (days 10–35). After day 35, as the flow becomes highly nonlinear, explanation for the behavior of the two-day wave modes on the basis of linear instability mechanisms fails. The (4, 1.89) mode amplification near days 38 and 52 does not occur in conjunction with its critical line overlapping the negative $\overline{q}_\varphi$ region. Moreover, the (3, 2.04) mode amplitude is conspicuously absent near day 40 even when the modes critical line crosses the shaded region. Nonlinear wave–mean flow interactions and possibly also wave–

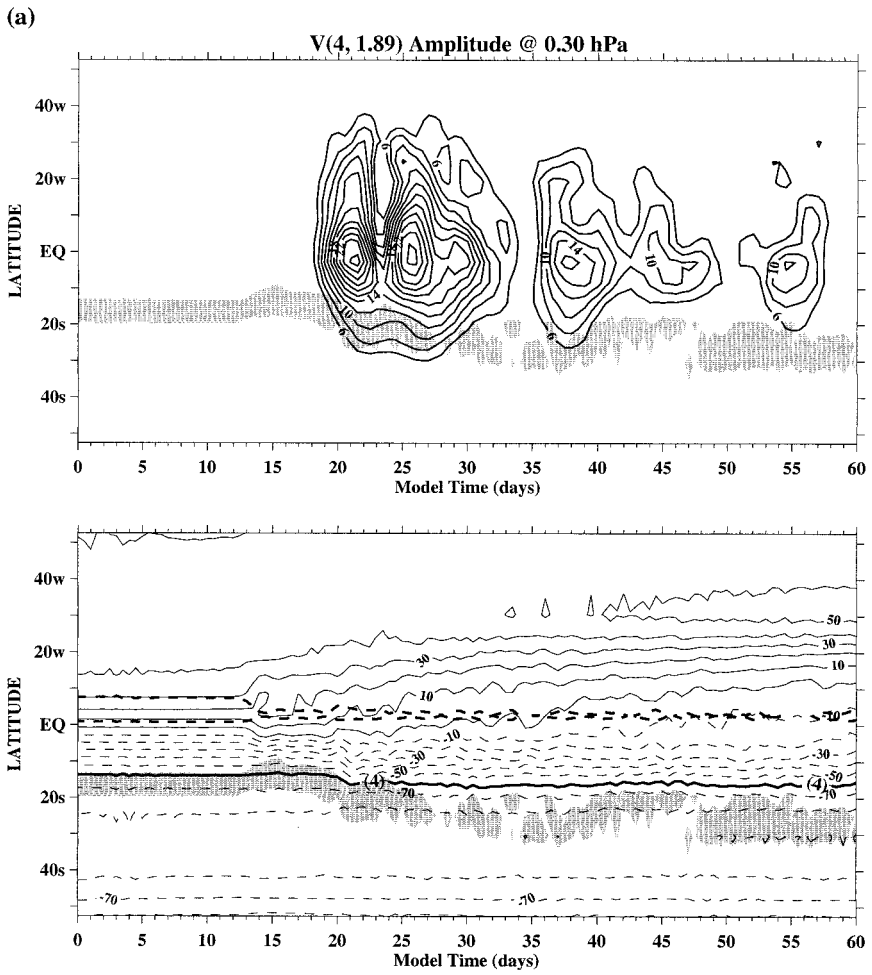

FIG. 6. (a) (top) The meridional wind (4, 1.89) amplitude evolution and (bottom) the zonal wind evolution at 0.3 hPa of the control run. The wind amplitude and the zonal wind are contoured every 2 and 10 m s^{-1}, respectively. The negative $\overline{q}_\varphi$ regions are shaded. In the bottom panel, the bold solid line, labeled with ''4,'' indicates the (4, 1.89) critical line, and the bold dashed line encloses areas of possible inertial instability.

wave interactions must be influencing the wave amplitude oscillations in the late phase of the model run.

5. Control run: Two-day wave triggering mechanism

Figure 6a shows that the initial (4, 1.89) amplitude growth is preceded by the collocation of its critical line with the negative $\overline{q}_\varphi$ region around days 13–20. Comparison of the upper panels of Figs. 1 and 5 shows that the negative $\overline{q}_\varphi$ region on the equatorward edge of the jet has broadened and deepened between days 0 and 15–25. The tightening of the easterly wind contours near 5° summer latitude (beginning around day 13) corresponds to an increase in positive horizontal wind curvature that is responsible for the enhanced negative $\overline{q}_\varphi$ region. To illustrate this, the zonal mean wind latitudinal profiles at 1.0 hPa are given in Fig. 7 (nearly identical wind profiles are seen at 0.3 hPa). Increased wind curvature commences around day 13 near 10° summer latitude and is facilitated by the transport of westerly momentum toward the summer hemisphere as made evident by the westerly wind deceleration near 10° winter latitude and acceleration near the equator on day 15. The increased horizontal wind curvature leads to the expansion of the initially prescribed $\overline{q}_\varphi$ region around days 13–20 from which the two-day wave components grow.

Momentum redistribution shown in Fig. 7 is remarkably similar to that associated with the inertial instability, both in theory (Dunkerton 1981) and in observations based on UKMO analyses (Fig. 9 of Orsolini et al. 1997). Indeed, in the control run, features reminiscent of inertial instability appear in low winter latitudes around days 10–14 just prior to the onset of westerly momentum transport toward the summer hemisphere. The EP flux diagram of the total wave field averaged between days 10 and 15 shows strong wave fluxes directed from an EP flux divergence region over the equa-

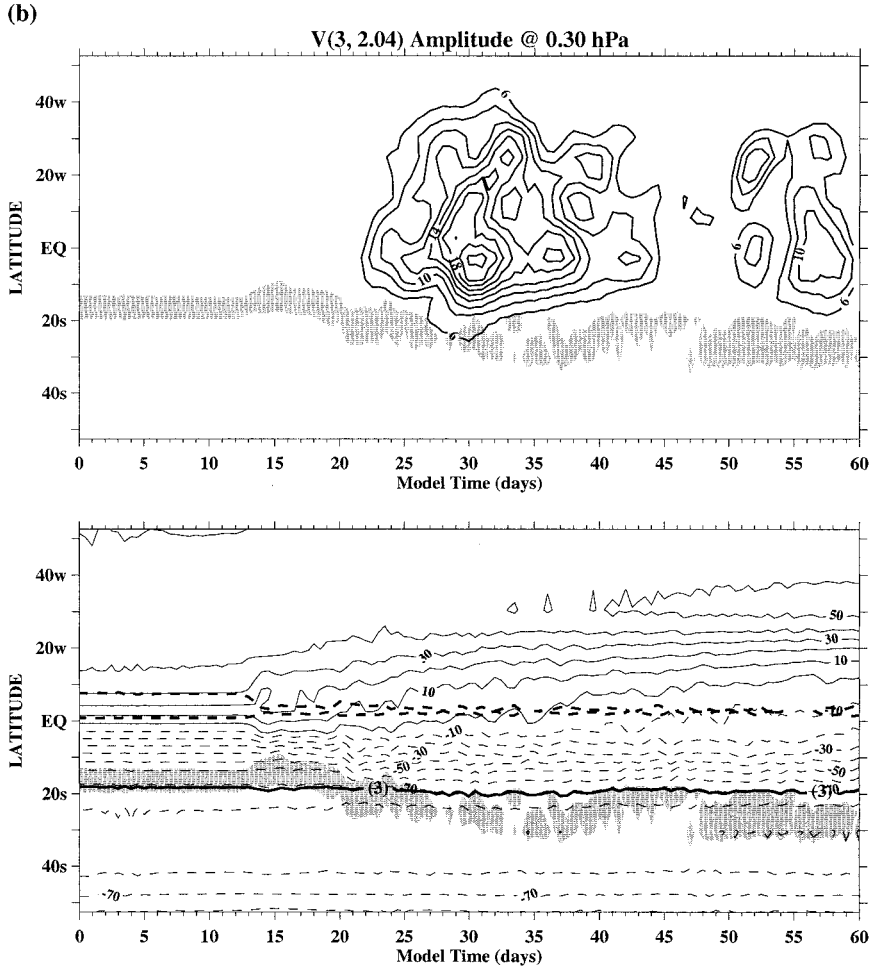

FIG. 6 *(Continued)* (b) Same as (a) except for the (3, 2.04) mode. Also, the bold line, labeled with "3," indicates the (3, 2.04) critical line.

tor toward a convergence region near 10° winter latitude (Fig. 8). This EP flux pattern closely resembles the pattern in Fig. 6b of Hitchman et al. (1987) who observed inertial instability features using estimated balance winds from LIMS temperature data. Additionally, the mean wind evolution also shows that during the period of increasing zonal wind curvature, the region of $f(f - a^{-1}\overline{u}_{\varphi}) < 0$ (where inertial instability is possible) simultaneously diminishes in size, as shown in Fig. 6. This suggests the removal of inertial instability by the momentum redistribution, which also barotropically destabilizes the easterly jet.

Structure of the features responsible for this momentum redistribution is illustrated in Figs. 9 and 10. These zonally asymmetric features do not develop in a 60-day model run without planetary wave forcing (e.g., $A = 0$). In addition to their momentum fluxes, these disturbances resemble disturbances observed by Hitchman et al. (1987) and Hayashi et al. (1998) and modeled by O'Sullivan and Hitchman (1992) and Sassi et al. (1993) in their 1) concentration in the winter tropical stratopause region where and when the background flow is inertially unstable, 2) low zonal wavenumber, 3) excitation by planetary Rossby waves, 4) vertical stacking characteristics, and 5) temperature anomalies of opposite sign in high and low latitudes.

However, the disturbance vertical scale seen in the satellite observations and verified by comparison with in situ rocket temperature measurements (Hitchman et al. 1987) is approximately 7 km, about twice that of our modeled inertial waves. Moreover, the observed meridional scale is somewhat larger, and the persistence of the observed disturbances is longer (as much as 1–2 weeks). Our model clearly does not properly represent the mechanism that controls the vertical scale, so our disturbances collapse to the model vertical grid scale. Differences in horizontal structure and persistence can be attributed to differences in forcing; in contrast to the range of Rossby waves and frequencies actually present, we force the Tropics with only a single smoothly equilibrating planetary wave. Despite these discrepancies, we conclude that the simulated inertial disturbances provide

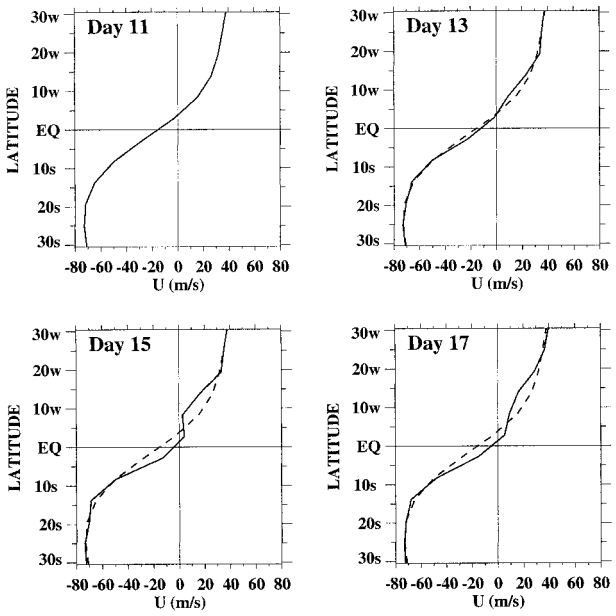

FIG. 7. The zonal mean zonal wind profile at 1.0 hPa of the control run. The dashed line shows the profile for day 11. The solid line shows the profile of the indicated day.

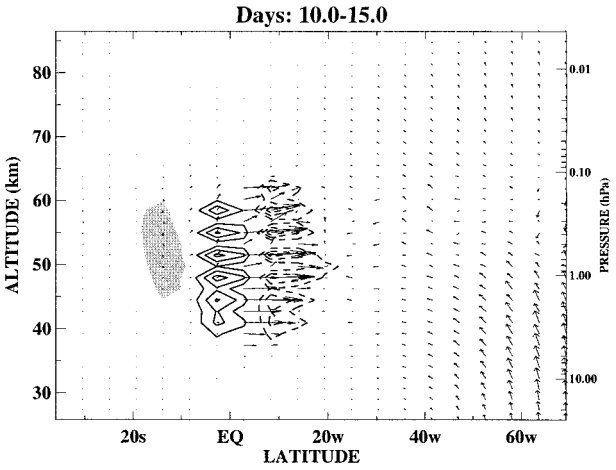

FIG. 8. Five-day-averaged cross sections of the EP flux (vector) and wave forcing per unit mass (EP flux divergence) of the control run. Contour interval is 1.0 m s^{-1} day^{-1} starting from 1.0 m s^{-1} day^{-1}. Solid (dashed) contours denote westerly (easterly) acceleration. Negative $\overline{q}_\varphi$ region is shaded.

a reasonable qualitative simulation of the effects of large-scale zonally asymmetric inertial instability on the zonal mean flow.

Thus, the simulated two-day wave appears to be initiated by wave disturbances similar to inertial instability organized by the forced winter planetary wave. The momentum redistribution by the simulated inertial waves can destabilize the mean flow in low summer latitudes where strong meridional wind shear was already present at day 0. The two-day wave growth (first the zonal wavenumber 4 then 3) is evident from the EP flux, which is directed away from the mode's critical line within the negative $\overline{q}_\varphi$ region. This wave triggering scenario is similar to that suggested by Orsolini et al. (1997) and observed in the 1992–93 austral summer by Limpasuvan et al. (2000).

6. Sensitivity runs

a. Variations of the control run

We also examine the sensitivity of the control run to a weakened Newtonian cooling profile with $(\alpha, \beta) = (1.5, 1.0)$ and to incrementally doubled winter Rossby wave forcing amplitude peak, A (see section 2). Except when the amplitude of the imposed wave is strong enough to cause complete reorganization of the winter hemisphere zonal winds (e.g., $A = 2940$ m^2 s^{-2}), results of these sensitivity runs closely resemble the results discussed above in that the simulated two-day wave appears as a barotropically unstable wave consistently initiated by the destabilization of the summer subtropical easterly jet, fostered by the simulated inertial in-

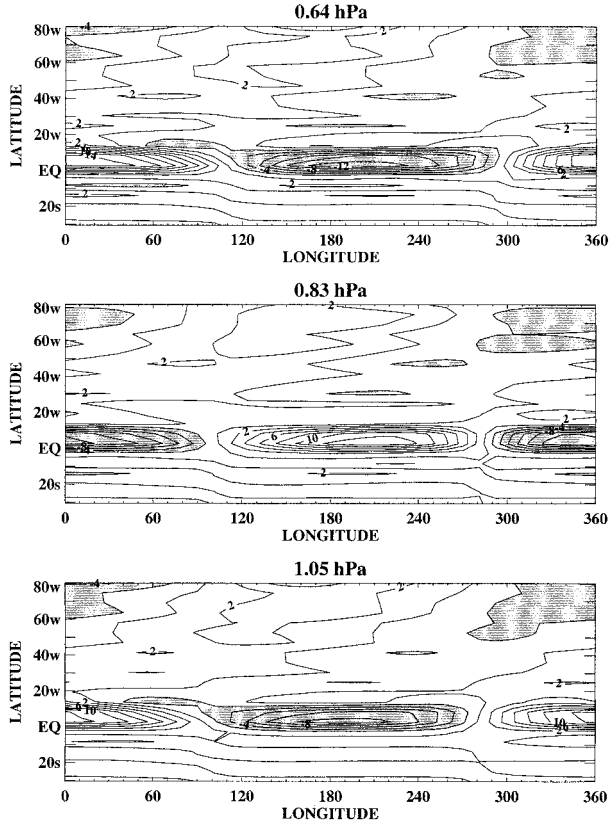

FIG. 9. Maps of meridional wind anomalies (zonal wavenumbers 1–10) at day 13 of the control run. The levels shown correspond to three consecutive model levels. The wind contours are in intervals of 2 m s^{-1} with anomalies less than -2 m s^{-1} shaded.

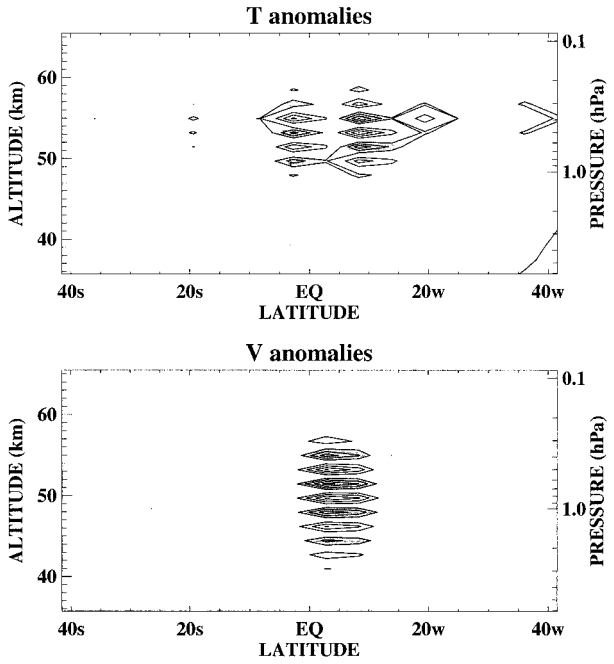

FIG. 10. (top) Cross-section structure of the temperature anomalies, and (bottom) meridional wind anomalies (zonal wavenumbers 1–10) at 180° longitude and day 13 of the control run. The temperature (meridional wind) anomalies are contoured every 0.6 K (3 m s^{-1}). Negative anomalies are shaded and the zero contour is removed for clarity.

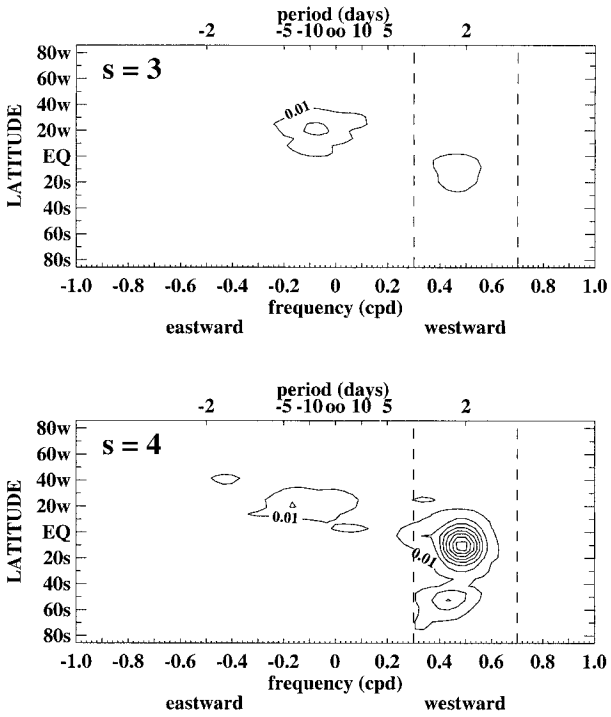

FIG. 11. The latitude–frequency structure of the temperature zonal wavenumber-3 and -4 spectra at 1.0 hPa of the weakened easterly jet case. The contours are given in increments of 0.05 K^2 day.

stability features. The two-day wave EP flux structure for these runs is generally similar to the control run (see Fig. 5). However, above 0.1 hPa for the weaker Newtonian cooling profile run, greater poleward and upward energy propagation of the wavenumber-3 mode is apparent. The stronger energy propagation in this case of weaker and probably more realistic radiative damping is consistent with the observed large amplitude of the wavenumber-3 mode above 0.1 hPa (see Wu et al. 1993).

When the forcing amplitude is set to zero, only symmetric inertial instability occurs and is initiated by weak zonally symmetric meridional circulation driven by the imposed Rayleigh friction. In fact, the model evolution remains zonally symmetric past 50 model days and no two-day wave develops. The zonally symmetric vertically stacked pattern has weaker extrema and persists for a long time before momentum redistribution can alleviate the inertially unstable condition. Futhermore, when the forcing Rossby wave amplitude is fixed but a wavenumber-2 structure is imposed, a zonal wavenumber-2 inertially unstable disturbance is evident. The overturning circulation is weaker than in the control case with the wavenumber-1 forcing but persists longer. As with the wavenumber-1 forcing, the two-day wave is triggered as the inertially unstable feature weakens. The modeled inertial instability features appear to be directly related to the meridional motions imposed by the winter Rossby wave forcing in agreement with the model studies of O'Sullivan and Hitchman (1992) and Sassi et al. (1993).

b. Simulation with weakened initial easterly jet

The control experiment is repeated with a new initial wind shown in Fig. 1b [see Limpasuvan (1998), for its analytical representation]. The easterly jet has now been weakened considerably so that the observed (3, 2.0) mode critical line is entirely removed, and only the observed (4, 1.8) critical line is supported in the summer subtropics. Despite the weak easterlies near the stratopause, the strong meridional wind shear is able to produce a region of negative $\overline{q}_{\varphi}$ in low summer latitudes. The westerly wind structure is identical to the initial condition shown in Fig. 1a, so it effectively guides the forced Rossby wave into the subtropical stratopause. Overall, the prescribed easterly wind strength is similar to the MLS-observed boreal summer conditions (July–August) shown in Limpasuvan et al. (2000).

Spectral analysis for days 10–39 shows that, unlike the control run, the zonal wavenumber-4 component dominates the two-day wave signal (Fig. 11). The wavenumber-3 spectral signature is much smaller than the wavenumber-4 signal whose major temperature disturbance is concentrated near 10° summer latitude with a lower frequency secondary maximum at summer midlatitudes. The wavenumber-3 and -4 spectral peaks are, respectively, at westward periods of 2.22 and 2.04 days.

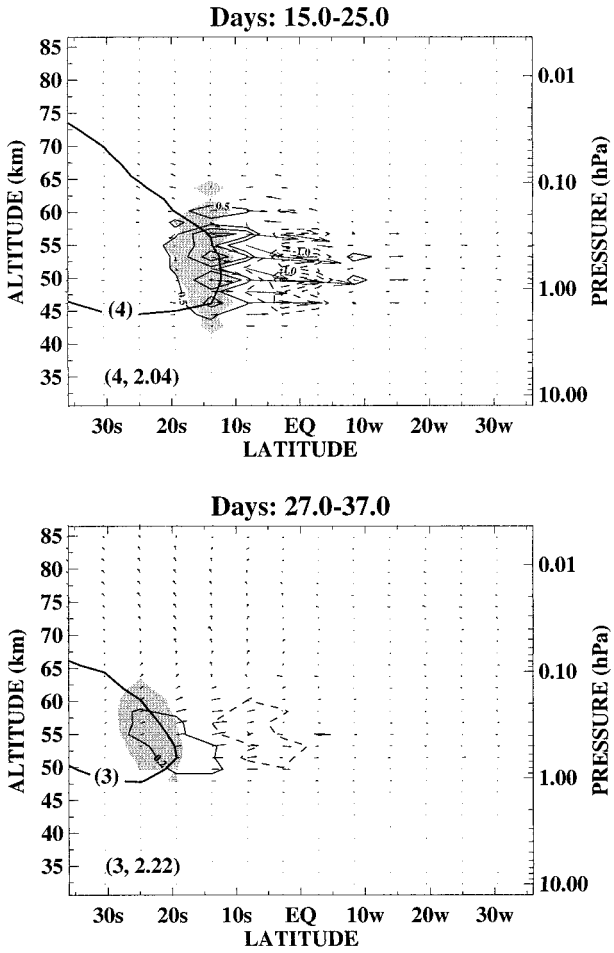

FIG. 12. The 10-day-averaged EP flux vectors diagrams (top) for the (4, 2.04) mode, and (bottom) the (3, 2.22) mode, of the weakened easterly jet case. The maximum vector length of each panel is scaled relative to the top panel of Fig. 5 (control run). The wave forcing per unit mass (EP flux divergence) is contoured every 0.5 m s^{-1} day^{-1} for the top panel and of 0.2 m s^{-1} day^{-1} for the bottom panel. Solid (dashed) contours denote westerly (easterly) acceleration. The shaded areas show the negative $\overline{q}_\varphi$ regions. The mode critical line is shown in the diagrams as a bold line and labeled with ''3'' and ''4'' for the (3, 2.22) and (4, 2.04) modes, respectively.

The cross-section structure (not shown) computed from bandpass filtering over westward frequency range 0.3–0.7 cpd resembles the control case (see Fig. 4), although the wavenumber-3 component amplitude is obviously much weaker.

The time-averaged, filtered EP flux vectors for the (3, 2.22) and (4, 2.04) modes again indicate that both modes arise from barotropic instability growth (see Fig. 12). Consistent, with the amplitude structure, the greatest (4, 2.04) EP flux occurs between 0.10 and 1.0 hPa and is mainly directed horizontally toward the winter hemisphere. The (3, 2.22) EP flux is similar but much weaker. The appearance of the wavenumber-3 mode as a barotropic instability wave is not suggested in the available two-day wave observations during the boreal summers (Wu et al. 1996; Limpasuvan et al. 2000).

As with the control run, inertial instability features precede the growth of the wavenumber-4 mode. The same sequence of wave and mean flow events discussed in the control run is again evident, and the initial instability wave growth (days 15–20), evident in the EP flux patterns, coincides with the intersection of the critical line and the negative $\overline{q}_\varphi$ region in the equatorward flank of the easterly jet (Fig. 12). However, in the MLS boreal summer data reported by Wu et al. (1996) and Limpasuvan et al. (2000), the observed wavenumber-4 component of the two-day wave appears to be related mainly to the baroclinic instability above the jet core, as suggested by Norton and Thuburn (1996, 1997). The observed boreal summer instability is seemingly well removed from the effects of momentum redistribution of inertial instability. It remains to be seen whether this is always the case during other boreal summers.

Another notable difference of the weakened easterly jet case from the control run is the slower phase speed of both two-day wave components. This difference ultimately results from the weaker initial wind field. As momentum redistribution by inertial instability expands the negative $\overline{q}_\varphi$ region into the low summer latitudes around day 15, the wavenumber-4 mode grows from the critical line source. In the control case, the easterly wind speed range within the negative $\overline{q}_\varphi$ region is 50–70 m s^{-1} over a deep layer around the stratopause (see Fig. 5). For the weakened easterly jet case, this easterly wind speed range is only 40–60 m s^{-1}. As the growing unstable mode has a critical line in the negative $\overline{q}_\varphi$ domain, the resulting mode phase speed is limited by the wind speed range of each case. Discrete unstable wave modes with different zonal phase speeds are selected in accordance with the relationship between zonal flow speed range and the negative $\overline{q}_\varphi$ region in each flow. The difference in speed ranges accounts for the slower wavenumber-4 mode in the present run as opposed to the control case. A similar argument applies to the growth and period of the wavenumber-3 mode in the model.

With the initially weaker easterly jet, this sensitivity run favors the wavenumber-4 mode of the two-day wave. The top and bottom panels of Fig. 13 show the two-day wave meridional wind amplitude for both the strong initial easterly jet (control case) and weakened initial jet runs. The amplitude is averaged vertically between 5 and 0.1 hPa and latitudinally between 40° summer latitude and 40° winter latitude. The (3, 2.22) mode is considerably weaker than the (4, 2.04) mode in the weakened easterly jet case, but nonetheless exhibits some weak upward–poleward energy propagation into the mesosphere (see Fig. 12). In this respect, the simulation agrees with the observed MLS boreal two-day wave that is dominated by the wavenumber-4 component. However, the observed wavenumber-4 mode during the boreal summer seasons has significantly higher frequency than the simulated wave. This difference is

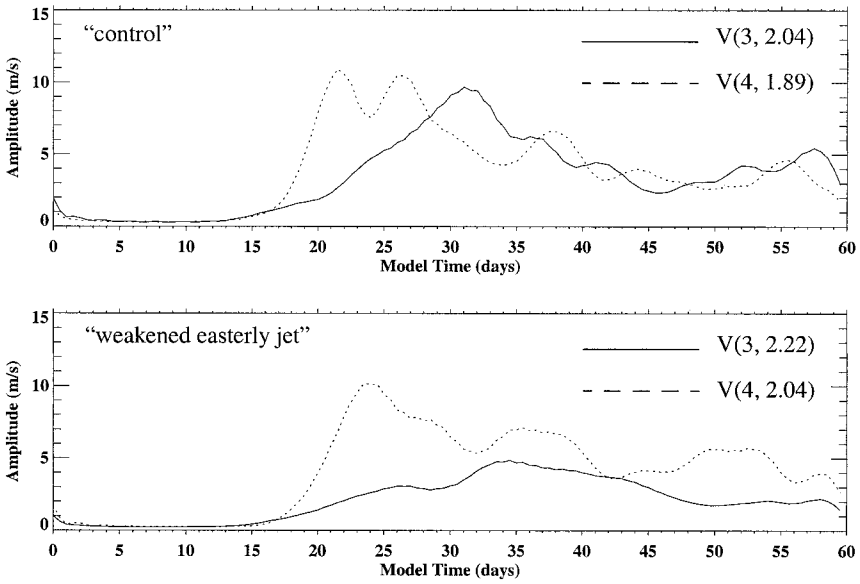

FIG. 13. The averaged meridional wind two-day wave amplitudes for winter planetary wave forcing of $A = 368$ m^2 s^{-2} of (top) the strong Newtonian cooling run (control case) and (bottom) the weakened initial easterly jet run. The wave amplitudes are averaged vertically from 5 to 0.1 hPa and latitudinally from 40° summer latitude to 40° winter latitude.

apparently because the defined initial wind field does not precisely emulate the actual boreal summer wind.

7. Summary and discussion

Using a mechanistic version of a middle atmosphere GCM, we simulated the two-day wave near the stratopause and lower mesosphere. Several features of the satellite-observed two-day wave during the austral summer (Burks and Leovy 1987; Wu et al. 1993, 1996; Limpasuvan et al. 2000) were well reproduced. The model results exhibit both components of the two-day wave (the wavenumber-3 and -4 modes) with their respective periods in good agreement with observations. The associated temperature wave has realistic amplitudes (2–3 K) that maximize near the stratopause and on the equatorward flank of the easterly jet. The corresponding meridional wind wave structure peaks over the equator and has a reasonable amplitude of 10–20 m s^{-1} in the upper stratosphere and lower mesosphere.

The modeled two-day wave appears to be mainly related to barotropic instability. The two-day wave EP flux is found to emanate from the critical line within the region of negative $\overline{q}_\varphi$, illustrating that conversion from the mean flow to wave activity is taking place along the critical line. Between 2 and 0.1 hPa, the EP fluxes of both two-day wave components are directed equatorward consistent with the modes' tendency to transfer westerly momentum into the easterly jet core. Above 0.1 hPa, wavenumber-3 energy propagates upward and poleward along the equatorward flank of the easterly jet. On the other hand, the wavenumber-4 energy propagation is found to be confined mainly near the stratopause as its upward propagation is greatly attenuated upon encountering strong dissipation in the mesosphere. This may be why the wavenumber-4 mode is usually reported only below 0.1 hPa (Burks and Leovy 1986; Wu et al. 1996; Limpasuvan et al. 2000).

Given a strong horizontal wind shear on the equatorward flank of the initial easterly jet and across the equator, the model results suggest triggering of the two-day wave by inertially unstable disturbances. Near the winter subtropical stratopause, the amplifying forced winter Rossby wave propagating into low winter latitudes interacts with the zonal mean flow in the inertially unstable region and organizes inertial instability circulation. Meridional cross-section structures of the simulated circulation resemble the ''pancake'' structures found in the LIMS and CLAES observations (Hitchman et al. 1987; Hayashi et al. 1998). Momentum readjustment associated with the inertial instability circulation then increases the horizontal wind curvature just equatorward of the easterly jet core by transporting westerly momentum equatorward. As a result of the increased horizontal curvature, the gradient of potential vorticity is reversed over a deep layer across the stratopause, barotropically destabilizing the easterly jet. The wavenumber-4 component of the simulated two-day wave grows first as a result of barotropic instability. As the wave saturates, it transfers westerly momentum toward the jet core and increases the wind curvature at higher summer latitude. The reversed gradient of potential vorticity region then also migrates toward the easterly jet core. Subsequently, the wavenumber-3 component is observed to grow from barotropic instability. Overall, the model results make plausible the connection be-

tween inertial instability and the two-day wave, as suggested in the 1992–93 austral summer case in Limpasuvan et al. (2000) and in the analysis of Orsolini et al. (1997).

We note that in the observations the robust structure associated with inertial instability is seen to be localized in a restricted longitude band (Hayashi et al. 1998; Hitchman et al. 1987). This band roughly coincides with the cross-equatorial excursion of a coherent anomalous potential vorticity (PV) tongue associated the winter planetary wave activity in the subtropics. With the onset of planetary wave breaking, the anomalous PV tongue is torn into smaller anomalous PV blobs identifiable by anticyclonic circulation cells with inertial overturning periods. As suggested by Orsolini et al. (1997) and shown in Fig. 7 of Hayashi et al. (1998) using the UKMO analyses, these ''secondary'' inertial instability structures appear to have horizontal scales not readily resolvable by satellite observations or in a low-resolution model such as the one used here.

In our model, we found large-scale inertial instability features to be associated with the winter planetary wave activity propagating into the equatorial region from high winter latitude. Unlike the satellite observations, these features are not localized, perhaps because our model is initialized from a zonally symmetric state. Such a state is likely to differ markedly from the condition under which inertial waves actually occur. If triggering of the two-day wave by inertial instability disturbance does occur in reality, our results suggest that large-scale momentum fluxes associated with the preliminary inertial waves will be responsible. In the model runs, as planetary wave breaking advanced, we did see some evidence for the smaller secondary inertial instability features displaced toward the winter hemisphere from the zonal wavenumber-3 and -4 anticyclonic gyres associated with the two-day wave. However, the detailed structure of our inertially unstable planetary waves is strongly limited by model resolution, especially in the vertical. Although the model vertical wavelength ($\sim$3.5 km) is not inconsistent with some observations, the two-gridpoint characteristic of the inertial waves implies that the model is probably not correctly simulating the mechanism that actually determines their vertical scale (see the discussion in Hitchman et al. 1986).

Varying thermal damping or winter wave forcing within reasonable bounds does not drastically change the two-day wave propagation pattern, amplitude structure, or the manner in which it is triggered. Consistent with linear theory, the amplitude of winter forcing has little or no effect on the amplitude of the unstable wave. In this sense, the winter forcing does not directly force the two-day wave, although, near the stratopause, the forced winter planetary wave is necessary to organize the triggering inertial instability. However, the two-day wave period can change because of the mean flow effect of the forcing variations.

Simulation with an initially weakened easterly jet has also been performed to emulate the observed boreal summer condition. The main model result is the suppression of the wavenumber-3 two-day wave in agreement with the observed tendency during the boreal summers (Wu et al. 1996; Limpasuvan et al. 2000). Given the strong initial equatorial wind shear, inertial instability again appears to trigger the two-day wave. However, this aspect of the model simulation may not emulate reality. In the MLS data as shown by Wu et al. (1996) and Limpasuvan et al. (2000), the unstable wave source appears near the jet core and far from the region that could be destabilized by inertial instability during the boreal summer. As a result, the strong wind speed near the core of the actual jet produces an unstable wavenumber-4 component that has a period nearly identical to its austral summer counterpart ($\sim$1.8 days). In the model, the weaker easterly jet in the barotropically unstable shear zone produces a slower wave period ($\sim$2.04 days). The combined sensitivity results with weaker initial easterly jet and varied forcing suggest that the weaker wavenumber-3 two-day wave component during the observed boreal summer reported by Wu et al. (1996) and Limpasuvan et al. (2000) is a consequence of weaker easterly jet strength.

Of all the observed features of the two-day wave that the model failed to generate, the most disturbing is the lack of wavenumber-3 component dominance in any of the runs. While the wavenumber-4 mode is reported to have greater amplitude than the wavenumber-3 during the boreal summer, the opposite is often observed during the austral summer, which was simulated in the control run. Our inability to simulate a dominant wavenumber-3 mode suggests that, although triggering of the two-day wave by inertially unstable disturbances is plausible, particularly during the austral summer, mechanisms other than those represented in the model may also be responsible for the wavenumber-3 excitation.

Acknowledgments. We thank three anonymous reviewers who helped improve the manuscript significantly and Drs. Charles McLandress, Takeshi Horinouchi, and M. Joan Alexander for useful conversations. This work was supported by NASA under Grant NAG5-3188 and is based in part on VL's Ph.D. dissertation at the University of Washington.

REFERENCES

Andrews, D. G., J. R. Holton, and C. B. Leovy, 1987: *Middle Atmospheric Dynamics.* Academic Press, 489 pp.

Boville, B. A., 1995: Middle atmosphere version of CCM2 (MACCM2): Annual cycle and interannual variability. *J. Geophys. Res.,* **100,** 9017–9039.

Burks, D., and C. B. Leovy, 1986: Planetary waves near the mesospheric easterly jet. *Geophys. Res. Lett.,* **13,** 193–196.

Charney, J. G., and P. G. Drazin, 1961: Propagation of planetary-scale disturbances from the lower into the upper atmosphere. *J. Geophys. Res.,* **66,** 83–109.

Dunkerton, T. J., 1981: On the inertial stability of the equatorial middle atmosphere. *J. Atmos. Sci.,* **38,** 2354–2364.

Hack, J. J., B. A. Boville, B. P. Briegleb, J. T. Kiehl, P. J. Rasch, and D. L. Williamson, 1993: Description of the NCAR Community Climate Model (CCM2). NCAR Tech. Note TN-382, National Center for Atmospheric Research, Boulder, CO, 108 pp.

Hayashi, H., M. Shiotani, and J. C. Gille, 1998: Vertically stacked temperature disturbances near the equatorial stratopause as seen in cryogenic limb array etalon spectrometer data. *J. Geophys. Res.,* **103,** 19 469–19 483.

Hayashi, Y., 1971: A generalized method of resolving disturbance into progressive and retrogressive waves by space Fourier and time cross-spectral analyses. *J. Meteor. Soc. Japan,* **49,** 125–128.

Hitchman, M. H., and C. B. Leovy, 1986: Evolution of the zonal mean state in the equatorial middle atmosphere during October 1978–May 1979. *J. Atmos. Sci.,* **43,** 3159–3176.

——, ——, J. C. Gille, and P. L. Bailey, 1987: Quasi-stationary zonally asymmetric circulations in the equatorial lower mesosphere. *J. Atmos. Sci.,* **44,** 2219–2236.

Limpasuvan, V., 1998: Tropical dynamics near the stratopause: The two-day wave and its relatives. Ph.D. dissertation, Department of Atmospheric Sciences, University of Washington, 209 pp. [Available from Dept. of Atmospheric Sciences, University of Washington, Box 351640, Seattle, WA 98195.]

——, C. B. Leovy, and Y. J. Orsolini, 2000: Observed temperature two-day wave and its relatives near the stratopause. *J. Atmos. Sci.,* **57,** 1689–1701.

Muller, H. G., and L. Nelson, 1978: A traveling quasi 2-day wave in the meteor region. *J. Atmos. Terr. Phys.,* **40,** 761–766.

Norton, W. A., and J. Thuburn, 1996: The two-day wave in a middle atmosphere GCM. *Geophys. Res. Lett.,* **23,** 2113–2116.

——, and ——, 1997: The mesosphere in the extended UGAMP GCM. *Gravity Wave Processes and Their Parametrization in Global Climate Models,* K. Hamilton, Ed., Vol. 50, Springer-Verlag, 383–401.

Orsolini, Y. J., V. Limpasuvan, and C. B. Leovy, 1997: The tropical stratopause in the UKMO assimilated analyses: Evidence for a 2-day wave and inertial circulations. *Quart. J. Roy. Meteor. Soc.,* **123,** 1707–1724.

O'Sullivan, D. J., and M. H. Hitchman, 1992: Inertial instability and Rossby wave breaking in a numerical model. *J. Atmos. Sci.,* **49,** 991–1002.

Plumb, R. A., 1983: Baroclinic instability at the summer mesosphere: A mechanism for the quasi-two-day wave? *J. Atmos. Sci.,* **40,** 262–270.

Ray, E. A., M. J. Alexander, and J. R. Holton, 1998: An analysis of the structure and forcing of the equatorial semiannual oscillation in zonal wind. *J. Geophys. Res.,* **103,** 1759–1774.

Salby, M. L., 1996: *Fundamentals of Atmospheric Physics.* Academic Press, 627 pp.

Sassi, F., R. R. Garcia, and B. A. Boville, 1993: The stratopause semiannual oscillation in the NCAR community climate model. *J. Atmos. Sci.,* **50,** 3608–3624.

Takahashi, M., and B. A. Boville, 1992: A three-dimensional simulation of the equatorial quasi-biennial oscillation. *J. Atmos. Sci.,* **49,** 1020–1035.

Vincent, R. A., 1984: MF/HF radar measurements of the dynamics of the mesopause region—A review. *J. Atmos. Terr. Phys.,* **11,** 961–974.

Wu, D. L., P. B. Hays, W. R. Skinner, A. R. Marshall, M. D. Burrage, R. S. Lieberman, and D. A. Ortland, 1993: Observations of the quasi 2-day wave from the high resolution Doppler imager on *UARS. Geophys. Res. Lett.,* **20,** 2853–2856.

——, E. F. Fishbein, W. G. Read, and J. W. Waters, 1996: Excitation and evolution of the quasi-2-day wave observed in *UARS*/MLS temperature measurements. *J. Atmos. Sci.,* **53,** 728–738.